

POP. III STARS FROM TURBULENT FRAGMENTATION AT REDSHIFT ~ 11

JOAQUIN PRIETO^{1,2}, PAOLO PADOAN¹, RAUL JIMENEZ¹, LEOPOLDO INFANTE²

Draft version March 21, 2022

ABSTRACT

We report results from a cosmological simulation with non-equilibrium chemistry of 21 species, including H₂, HD, and LiH molecular cooling. Starting from cosmological initial conditions, we focus on the evolution of the central 1.8 Kpc region of a $3 \times 10^7 M_{\odot}$ halo. The crossing of a few $10^6 M_{\odot}$ halos and the gas accretion through larger scale filaments generate a turbulent environment within this region. Due to the short cooling time caused by the non-equilibrium formation of H₂, the supersonic turbulence results in a very fragmented mass distribution, where dense, gravitationally unstable clumps emerge from a complex network of dense filaments. At $z = 10.87$, we find approximately 25 well defined, gravitationally unstable clumps, with masses of $4 \times 10^3 - 9 \times 10^5 M_{\odot}$, temperatures of approximately 300 K, and cooling times much shorter than the free-fall time. Only the initial phase of the collapse of individual clumps is spatially resolved in the simulation. Depending on the density reached in the collapse, the estimated average Bonnor-Ebert masses are in the range 200 – 800 M_{\odot} . We speculate that each clump may further fragment into a cluster of stars with a characteristic mass in the neighborhood of 50 M_{\odot} . This process at $z \approx 11$ may represent the dominant mode of Pop. III star formation, causing a rapid chemical enrichment of the protogalactic environment.

Subject headings: cosmology: large-scale structure of universe, galaxies: formation, stars: formation – turbulence

1. INTRODUCTION

The primordial (Pop. III) star formation process has been extensively studied in the last decade by a number of authors (Abel et al. 2000, 2002; Bromm et al. 1999, 2002; Yoshida et al. 2006; McGreer & Bryan 2008), who have concluded that primordial stars of masses in the range $\sim 10^2 - 10^3 M_{\odot}$ are formed in dark matter (DM) mini halos of $\sim 10^6 M_{\odot}$ at a redshift of $z \sim 30 - 15$. Although in the collapse of such mini halos turbulent motions seem not to be important, at least on scales comparable to their virial radius, they are important for larger halos and may play a key role in the star formation process at high redshift, as in present-day star formation (Padoan et al. 2007).

Wise & Abel (2007) and Greif et al. (2008) have discussed the generation of turbulent motions in primordial gas through the virialization process of haloes of mass $\sim 10^7 M_{\odot}$. They have shown that the collapse of primordial gas on such halos, and particularly the cold accretion through filaments, generate supersonic turbulent motions, which partially ionize the primordial gas allowing an efficient formation of H₂ and HD molecules and efficient cooling to a gas temperature of $\sim 200 - 300$ K. They have argued that these turbulent, low temperature regions could be sites of efficient star formation. However, their simulations do not spatially resolve the fragmentation process to the scale of individual dense clumps associated with star-forming regions, and adopt adaptive mesh refinement (AMR) and smooth particle hydrodynamics (SPH) methods that were not specifically designed to resolve well the turbulent cascade within the

central 1.8 Kpc region.

In this letter, we present the results of an N-body and hydrodynamical simulation with non-equilibrium chemistry and cooling (including H₂, HD, and LiH cooling), carried out with the cluster Geryon at the AIUC-PUC. Starting from cosmological initial conditions, the simulation focuses on the evolution of the central 1.8 Kpc region of a $3 \times 10^7 M_{\odot}$ halo. A uniform mesh of 512^3 computational cells in that region provides a uniform spatial resolution of 3.5 pc, which allows us to follow the generation of turbulent motions in the primordial gas by the combined effects of the crossing of a few $10^6 M_{\odot}$ halos and of the gas accretion through larger scale filaments. The turbulence results in the formation of a large number of gravitationally unstable clumps at $z \approx 11$, with a characteristic mass of $10^5 M_{\odot}$. These clumps may be sites of efficient star formation in primordial gas, well before the virialization process of the first galaxies.

2. METHODOLOGY

We used the AMR code RAMSES (Teyssier 2002) with a modified non-equilibrium cooling module with 21 species (including H₂, HD, and LiH molecules with their cooling functions) in order to follow the thermochemical evolution and the gravitational collapse of primordial gas. All chemical reaction rates were taken from Stancil et al. (1996), Galli & Palla (1998), and Glover & Abel (2008).

We worked in a concordance Λ CDM cosmological model: $h = 0.72$, $\Omega_{\Lambda} = 0.73$, $\Omega_m = 0.27$, $\Omega_b = 0.04$, $\sigma_8 = 0.9$ and $n_s = 0.95$. The dynamical initial conditions were taken from mprgrafic (Prunet et al. 2008) and the initial chemical abundances were taken from Galli & Palla (1998) at $z = 120$ (the initial redshift of the simulation).

We first simulated a volume of $1 (\text{Mpc}/h)^3$ of only DM, with 256^3 particles. Using the HOP algorithm (Eisen-

¹ ICREA & ICC, University of Barcelona (IEEC-UB), Marti i Franques 1, E08028, Barcelona, Spain

² Centro de Astro-Ingenieria & Departamento de Astronomía y Astrofísica, Pontificia Universidad Católica de Chile, Vicuña Mackenna 4860, 7820436 Macul, Santiago, Chile

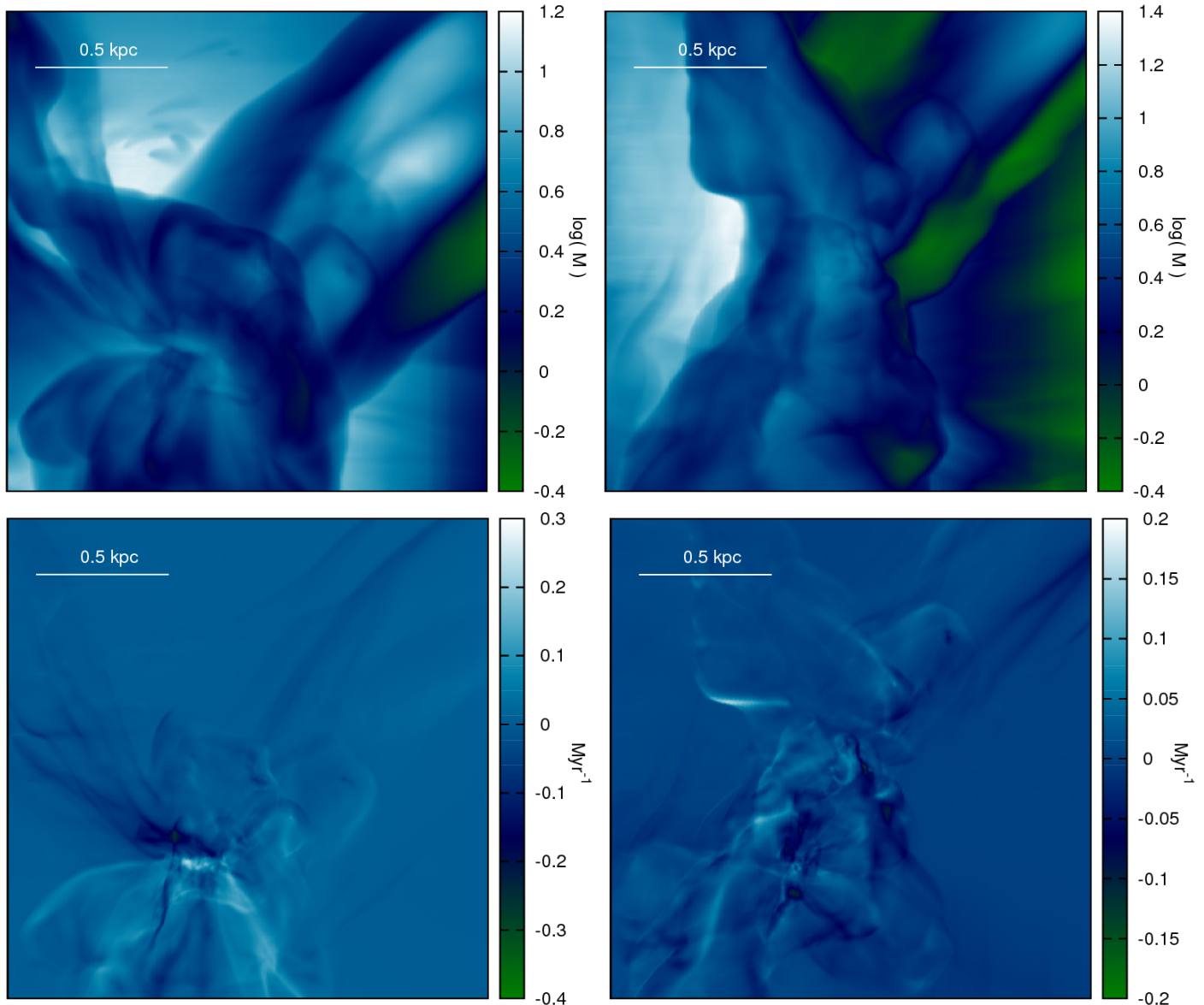


FIG. 1.— Upper panels: Line-of-sight gas rms velocity, averaged along the y direction (left) and z direction (right), divided by the sound speed averaged along the line of sight. Only the central region of the simulation is shown, where the uniform resolution mesh of 512^3 zones covers a size of 1.8 Kpc at $z = 10.87$. Lower panels: Average value of the vorticity component parallel to the line of sight for the same regions shown in the top panels.

stein & Hut 1998), we identified a $3 \times 10^7 M_\odot$ halo at $z = 10$. In order to better resolve the formation of that halo and to study its baryon component, we re-simulated the same $1 (\text{Mpc}/h)^3$ volume with 512^3 particles (with a particle mass of approximately $800 M_\odot$), including gas with non-equilibrium primordial chemistry from the beginning of the simulation, at $z=120$. The gas dynamics was computed on a root grid of 64^3 computational zones, which was geometrically refined towards the center, increasing the spatial resolution by a factor of two within the central $1/8$ of the volume. This refinement criterion was applied three times, generating 4 nested meshes (including the root grid), each with 64^3 computational cells.

Inside the innermost 64^3 mesh, the gas dynamics was computed using 6 extra levels of adaptive mesh refinement, according to four different criteria: i) Lagrangian refinement based on the number density of DM parti-

cles (a finer refinement level is created in cells containing more than 4 DM particles), ii) Lagrangian refinement based on the baryonic mass density, iii) refinement based on the gas pressure gradient (for $\Delta p/p \geq 2$), and iv) refinement based on the Jeans' length, to satisfy Truelove's condition (Truelove et al. 1997). The pressure gradient criterion was included in order to better resolve the turbulent flow, as discussed in (Kritsuk et al. 2006). The three geometrical refinement levels, plus the additional 6 AMR levels, give an effective spatial resolution corresponding to that achieved by a uniform mesh of $32, 768^3$ computational elements, and corresponding to a proper size of 3.5 pc at $z = 10.87$.

This setup was used from the beginning of the simulation, at $z = 120$, until $z = 50$. At $z = 50$, another geometrical refinement criterion was added (while maintaining the others): Uniform spatial resolution corresponding

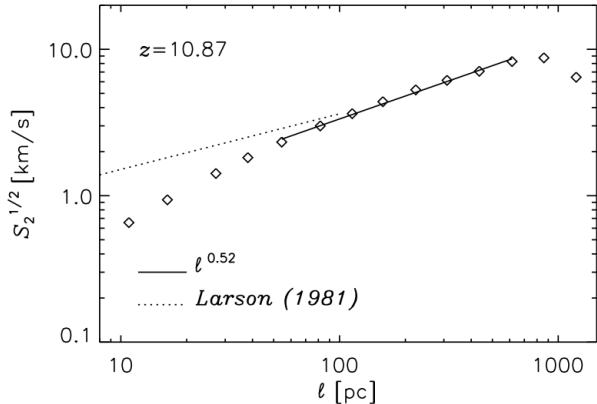


FIG. 2.— Square root of the second order longitudinal velocity structure function at redshift $z = 10.87$. The solid line shows the power-law fit in the range of scales (60–600 pc) where the structure function is well approximated by a power law. The dotted line corresponds to the size-velocity relation found by Larson (1981) in local Galactic molecular clouds.

to the highest refinement level was imposed in a volume centered approximately around the densest region of the halo, creating a uniform mesh of 512^3 elements. This uniform mesh, covering a proper size of 1.8 Kpc at $z = 10.87$, served the purpose of better resolving the generation of turbulent motions in the central region of the halo. The results presented in this work are based on the analysis of this central 1.8 Kpc region at the end of the simulation, corresponding to $z = 10.87$.

3. SUPERSONIC TURBULENCE

At a redshift of $z = 10.87$, gas turbulence is well developed in the central 1.8 Kpc region of the halo, and its supersonic motions have already created a complex network of dense filaments and clumps. The turbulence is driven by gas accretion from various large-scale filaments (extending well outside of the 1.8 Kpc region) and by the crossing of a few smaller DM halos, with masses of approximately $10^6 M_\odot$. The upper panels of Figure 1 show the rms line-of-sight velocity divided by the mean sound speed for each line of sight. The Mach number associated with this one-dimensional component of the velocity is typically $M_s \sim 3$, so the three-dimensional turbulent velocity has a characteristic value of $M_s \sim 5$. The supersonic turbulence creates a complex network of shocks, where vortical motion is generated. The lower panels of Figure 1 show the average value of the vorticity component parallel to the line of sight. One can see small-scale motion with characteristic timescales of 10 Myr.

Although the large-scale velocity field is driven primarily by the gravitational potential of the DM and baryons, the complexity of the collapse geometry appears to be sufficient to feed a turbulent cascade. A Helmholtz decomposition of the velocity field shows that the kinetic energy associated with solenoidal motions ($\nabla \cdot \mathbf{u} = 0$) is approximately three times larger than the kinetic energy of compressible motions ($\nabla \times \mathbf{u} = 0$), not too different from what is found in the inertial range of scales of isothermal turbulence driven by an incompressible force (Nordlund & Padoan 2003; Federrath et al. 2009; Kritsuk et al. 2009).

To further characterize the turbulence, we compute the

second order velocity structure function. The velocity structure function of order p is defined as:

$$S_p(\ell) = \langle |u(\mathbf{x} + \ell) - u(\mathbf{x})|^p \rangle \propto \ell^{\zeta(p)} \quad (1)$$

where the velocity component u is parallel (longitudinal structure function) or perpendicular (transversal structure function) to the vector ℓ , the spatial average is over all values of the position \mathbf{x} , and $\zeta(p)$ is the exponent of a power law fit to the structure function. The second order longitudinal structure function averaged in the central region of the simulation at $z = 10.87$ is plotted in Figure 2. It is well approximated by a power law, $\ell^{1.04}$, in the range of scales $\ell = 60 - 600$ pc. At smaller scales, the structure function becomes steeper, due to numerical diffusion; at larger scales it reaches a peak, probably indicative of a characteristic outer scale of approximately 600 pc, above which the filamentary gas accretion does not generate turbulent motions (consistent with the Mach number and vorticity maps of Figure 1). The slope of the structure function, $\zeta(2) = 1.04$, is a bit steeper than the value of $\zeta(2) = 0.95$ found in high-resolution simulations of randomly driven supersonic turbulence (Kritsuk et al. 2007). However, this can be mostly a consequence of the rather diffusive Ramses solver used for the simulation (the Local Lax-Friedrich Riemann solver with ‘minmod’ slope limiter), which is known to generate steeper velocity scaling than less diffusive solvers available in Ramses (but generally unstable with supersonic turbulence and self-gravity).

In order to relate this result with the observed properties of local Galactic star-forming regions, Figure 2 actually shows the square root of the second order structure function, next to the velocity scaling law found in Galactic molecular clouds (Larson 1979, 1981). Interestingly, on the scale of approximately 100 pc, the velocity dispersion in the primordial gas of our simulation is comparable to that of the molecular gas in our Galaxy. However, due to the larger temperature in the primordial gas, the Mach number of the turbulence is a few times smaller than in nearby molecular clouds at the same scale.

4. GRAVITATIONALLY UNSTABLE CLUMPS

Several dense clumps are found at the final redshift of the simulation, $z = 10.87$, with only two being clearly related to local over-densities of DM particles. These clumps are the direct result of the supersonic turbulence generated by the gas accretion into the central region of the halo. The turbulence creates a network of interacting shocks, forming dense intersecting filaments. The densest regions of this complex density field may be gravitationally unstable and result in collapsing clumps. The upper panels of Figure 3 show the mass weighted gas number density at $z = 10.87$, averaged along the y (left panel) and the z (right panel) directions. Over 20 well defined clumps can be seen, reaching densities above 10^4 cm^{-3} . As shown in the lower panels of the same Figure 3, these clumps are very effectively cooled down to temperatures of approximately 300 K.

In order to study the properties of these clumps, we have selected gravitationally unstable clumps using the clumpfind algorithm of Padoan et al. (2007). In this algorithm, clumps are defined as connected overdensities that cannot be split into two or more overdensities. The unstable ones are simply those with mass larger than

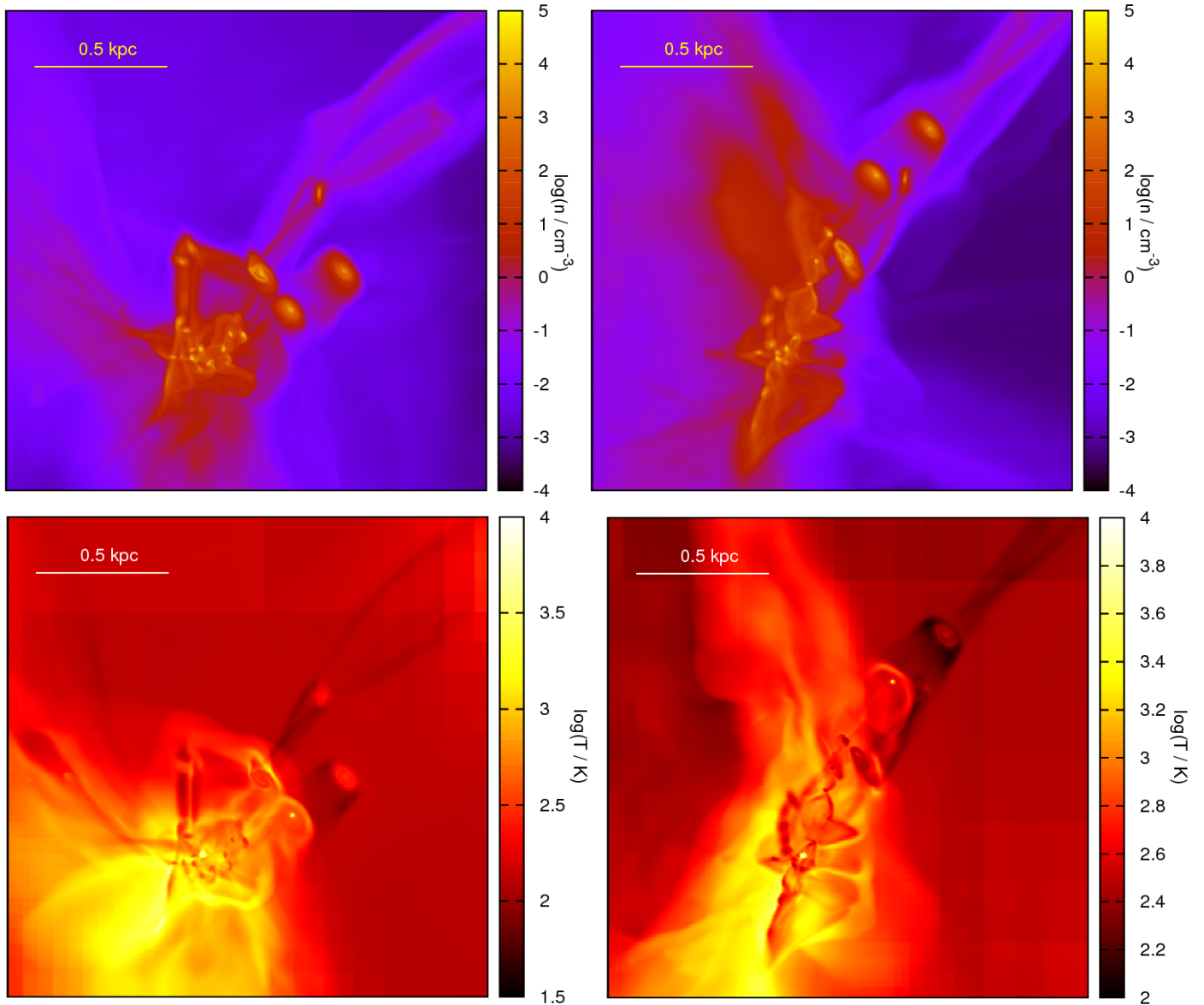


FIG. 3.— Upper panels: Mass weighted gas number density at $z = 10.87$, in the central region of the simulation covered by the uniform resolution mesh of 512^3 zones, averaged along the y (left panel) and the z (right panel) directions. Lower panels: Gas temperature averaged along the line of sight for the same regions shown in the upper panels (and in Figure 1). Several well-defined cores can be seen, with $n \sim 10^4 \text{ cm}^{-3}$ and $T \sim 300 \text{ K}$.

their Bonnor-Ebert mass. These definitions are implemented in the clumpfind algorithm by scanning the density field with discrete density levels, each a factor f larger than the previous one. Only the connected regions above each density level that are larger than their Bonnor-Ebert mass are selected as unstable clumps. After this selection, the unstable clumps from all levels form a hierarchy tree, of which only the final (unsplit) clump of each branch is retained.

The result of the clumpfind algorithm may be sensitive to the value of the parameter f (the density resolution), but in this case the cores are all so well defined that the same clumps are always selected for a wide range of values of f . Results given here are for $f = 2.0$. The other parameter of the algorithm is the minimum density. We have verified that the results have a weak dependence also on this parameter, for minimum densities

in the range $50\text{--}500 \text{ cm}^{-3}$, because most clumps are very well defined and relatively isolated overdensities. Results given here are for a minimum density of 400 cm^{-3} .

The clumpfind algorithm selects 25 gravitationally unstable clumps. All the dense clumps seen in Figure 3 are therefore gravitationally unstable. They account for 29% of the total baryonic mass of $1.97 \times 10^7 M_\odot$ found in the central 1.8 Kpc region (the DM mass in the same region is $1.89 \times 10^7 M_\odot$). The properties of these clumps are listed in Table 1. They are all cold, with temperatures of approximately 300 K, except for the first and the fourth of the list. The warmest of these two clumps is very clearly associated with a DM halo of approximately $10^6 M_\odot$. The Table also shows that the clump masses (excluded the first one that is most clearly associated to a mini-halo) are in the range $4.2 \times 10^3 \text{--} 7.3 \times 10^5 M_\odot$, while their Bonnor-Ebert masses

TABLE 1
AVERAGED CORE PHYSICAL QUANTITIES.

| Mass (M_{\odot}) | BE Mass (M_{\odot}) | n (cm^{-3}) | T (K) | $n_{\text{H}_2}/n_{\text{H}}$ | $n_{\text{HD}}/n_{\text{H}}$ | $n_{\text{LiH}}/n_{\text{H}}$ | $\Lambda_{\text{HD}}/\Lambda_{\text{H}_2}$ | $\Lambda_{\text{LiH}}/\Lambda_{\text{H}_2}$ | t_{cool} (yr) | $t_{\text{cool}}/t_{\text{ff}}$ |
|-------------------------|----------------------------|---------------------------|----------|-------------------------------|------------------------------|-------------------------------|--|---|---------------------------|---------------------------------|
| 8.78 (5) ^a | 3.17 (4) | 3.04 (3) | 6.55 (3) | 6.93 (-4) | 3.77 (-8) | 4.54 (-19) | 4.43 (-4) | 2.38 (-15) | 4.30 (3) | 5.08 (-3) |
| 7.33 (5) | 3.63 (2) | 2.97 (3) | 3.30 (2) | 1.82 (-2) | 1.87 (-6) | 4.98 (-19) | 4.66 (-2) | 2.66 (-15) | 1.15 (4) | 1.34 (-2) |
| 7.25 (5) | 2.61 (2) | 3.37 (3) | 2.76 (2) | 2.36 (-2) | 2.19 (-6) | 4.89 (-19) | 6.79 (-2) | 3.94 (-15) | 1.40 (4) | 1.74 (-2) |
| 5.81 (5) | 8.17 (3) | 1.54 (3) | 2.11 (3) | 1.65 (-3) | 9.13 (-8) | 2.30 (-19) | 3.29 (-4) | 1.21 (-16) | 2.31 (3) | 1.94 (-3) |
| 5.15 (5) | 2.59 (2) | 2.72 (3) | 2.56 (2) | 2.59 (-2) | 3.41 (-6) | 4.08 (-19) | 1.01 (-1) | 3.26 (-15) | 1.62 (4) | 1.82 (-2) |
| 3.40 (5) | 4.58 (2) | 1.20 (3) | 2.85 (2) | 7.63 (-3) | 8.53 (-7) | 2.02 (-19) | 4.40 (-2) | 2.30 (-15) | 5.77 (4) | 4.28 (-2) |
| 3.02 (5) | 5.84 (2) | 1.53 (3) | 3.63 (2) | 5.70 (-3) | 4.82 (-7) | 3.11 (-19) | 2.16 (-2) | 2.57 (-15) | 3.64 (4) | 3.05 (-2) |
| 2.79 (5) | 3.91 (2) | 2.28 (3) | 3.18 (2) | 1.15 (-2) | 1.19 (-6) | 4.02 (-19) | 4.44 (-2) | 3.22 (-15) | 2.21 (4) | 2.26 (-2) |
| 2.65 (5) | 3.58 (2) | 2.62 (3) | 3.13 (2) | 1.50 (-2) | 1.48 (-6) | 4.25 (-19) | 4.73 (-2) | 2.99 (-15) | 1.68 (4) | 1.84 (-2) |
| 2.49 (5) | 5.12 (2) | 1.08 (3) | 2.96 (2) | 7.27 (-3) | 6.19 (-7) | 1.54 (-19) | 2.91 (-2) | 1.53 (-15) | 5.76 (4) | 4.05 (-2) |
| 1.31 (5) | 5.05 (2) | 1.38 (3) | 3.18 (2) | 5.97 (-3) | 5.67 (-7) | 2.34 (-19) | 3.12 (-2) | 2.60 (-15) | 5.16 (4) | 4.11 (-2) |
| 1.23 (5) | 4.79 (2) | 1.09 (3) | 2.84 (2) | 4.97 (-3) | 5.85 (-7) | 1.77 (-19) | 4.45 (-2) | 2.96 (-15) | 9.33 (4) | 6.59 (-2) |
| 1.13 (5) | 6.06 (2) | 9.42 (2) | 3.17 (2) | 3.34 (-3) | 2.99 (-7) | 1.50 (-19) | 2.49 (-2) | 2.48 (-15) | 1.13 (5) | 7.40 (-2) |
| 8.55 (4) | 4.99 (2) | 1.50 (3) | 3.25 (2) | 5.40 (-3) | 5.25 (-7) | 2.70 (-19) | 3.19 (-2) | 3.29 (-15) | 5.20 (4) | 4.32 (-2) |
| 6.57 (4) | 6.24 (2) | 6.73 (2) | 2.89 (2) | 2.31 (-3) | 2.70 (-7) | 1.08 (-19) | 3.50 (-2) | 2.95 (-15) | 2.49 (5) | 1.38 (-1) |
| 6.29 (4) | 2.42 (2) | 4.63 (3) | 2.92 (2) | 2.69 (-2) | 2.57 (-6) | 6.92 (-19) | 7.40 (-2) | 5.25 (-15) | 9.75 (3) | 1.42 (-2) |
| 5.73 (4) | 7.19 (2) | 7.60 (2) | 3.30 (2) | 2.17 (-3) | 2.32 (-7) | 1.91 (-19) | 2.49 (-2) | 3.89 (-15) | 1.74 (5) | 1.03 (-1) |
| 5.57 (4) | 3.94 (2) | 6.83 (2) | 2.14 (2) | 3.60 (-3) | 7.78 (-7) | 1.02 (-19) | 1.28 (-1) | 4.75 (-15) | 3.45 (5) | 1.93 (-1) |
| 5.48 (4) | 6.36 (2) | 7.65 (2) | 3.05 (2) | 2.51 (-3) | 2.92 (-7) | 1.58 (-19) | 3.23 (-2) | 3.52 (-15) | 1.84 (5) | 1.09 (-1) |
| 3.14 (4) | 2.62 (2) | 3.63 (3) | 2.83 (2) | 1.96 (-2) | 2.11 (-6) | 5.57 (-19) | 7.78 (-2) | 5.28 (-15) | 1.53 (4) | 1.98 (-2) |
| 2.85 (4) | 7.44 (2) | 6.79 (2) | 3.25 (2) | 1.62 (-3) | 1.80 (-7) | 1.67 (-19) | 2.55 (-2) | 4.51 (-15) | 2.58 (5) | 1.44 (-1) |
| 2.21 (4) | 9.70 (2) | 4.84 (2) | 3.47 (2) | 8.72 (-4) | 8.83 (-8) | 1.44 (-19) | 1.81 (-2) | 5.32 (-15) | 5.07 (5) | 2.39 (-1) |
| 2.11 (4) | 3.39 (2) | 1.90 (3) | 2.72 (2) | 1.16 (-2) | 1.24 (-6) | 2.86 (-19) | 5.97 (-2) | 3.32 (-15) | 3.59 (4) | 3.35 (-2) |
| 1.42 (4) | 7.86 (2) | 5.00 (2) | 3.05 (2) | 1.37 (-3) | 1.67 (-7) | 1.20 (-19) | 2.92 (-2) | 4.16 (-15) | 4.38 (5) | 2.10 (-1) |
| 4.20 (3) | 3.47 (2) | 1.70 (3) | 2.66 (2) | 1.06 (-2) | 1.20 (-6) | 2.56 (-19) | 6.23 (-2) | 3.25 (-15) | 4.32 (4) | 3.82 (-2) |

^aA (B) \equiv A $\times 10^B$

span the limited range 200 – 800 M_{\odot} (excluding the two warmest clumps). Therefore, the clumps contain typically 100 to 1000 Bonnor-Ebert masses, suggesting the possibility of further fragmentation.

Table 1 also shows that H_2 is by far the dominant cooling agent, and that the cooling time is always orders of magnitude shorter than the free-fall time. The clumps are selected here at a single snapshot in time, and thus each of them is captured at a different phase of its evolution. However, based on the ratio of cooling to free-fall time, all the cores are expected to be able to collapse further, unless virialized by their internal fragmentation.

5. STAR FORMATION IN PRIMORDIAL GAS

This simulation describes the process of turbulent fragmentation of primordial gas in the central region of a $3 \times 10^7 M_{\odot}$ halo. Gravitationally unstable clumps are barely resolved, and we can only speculate about their fragmentation into stars. Their characteristic mass and densities are not much larger than those of giant molecular clouds (GMCs) in the Milky Way. Although their internal turbulence is not resolved in the simulation, Figure 2 shows that, based on the second order velocity structure function, the velocity dispersion should be comparable to that of nearby GMCs. Turbulent GMCs with an rms Mach number of $M_s \approx 20$ form stars with an initial mass function (IMF) that peaks at a mass approximately 20 times smaller than the average Bonnor-Ebert mass. This is understood as the result of the process

of turbulent fragmentation, where regions much denser than the mean are created by the supersonic flow, allowing local values of the Bonnor-Ebert mass much smaller than the mean value (Padoan et al. 1997; Padoan & Nordlund 2002; Padoan et al. 2007).

The primordial gas in the dense clumps found in the simulation has a characteristic temperature 30 times larger than nearby GMCs, so the rms Mach number could be approximately 5 times smaller, $M_s \approx 4$. This would imply a characteristic stellar mass a few times smaller than the average Bonnor-Ebert mass, or approximately 50 M_{\odot} for the densest clumps. Assuming a star formation efficiency of 10%, a $10^5 M_{\odot}$ clump of primordial gas would possibly fragment into a stellar cluster containing approximately 200 stars with masses in the neighborhood of 50 M_{\odot} (and many more stars of smaller mass). Because the characteristic stellar mass is some fraction of the mean Bonnor-Ebert mass, one cannot rule out the possibility of even smaller values that could arise if the clumps could collapse to a much higher density before fragmenting into stars, as illustrated for example in the recent work by Clark et al. (2011).

The details of this scenario of star formation in primordial gas are very uncertain at this stage, and can only be investigated with simulations of much larger spatial resolution. However, the results of this simulation shows that approximately one third of the primordial gas in the center of halos of a few $10^7 M_{\odot}$ is readily converted into gravitationally unstable clumps, very likely sites of

efficient star formation. This process occurring at a redshift of $z \approx 11$ may represent the dominant mode of Pop. III star formation, causing a rapid chemical enrichment of the protogalactic environment. Due to this early metal enrichment, star formation triggered by the assembly process of larger halos, at $z \approx 2 - 4$, will then be characterized by even shorter cooling times, lower tem-

peratures, and larger turbulence Mach numbers, yielding stellar masses already comparable to those of present-day star formation environments.

The simulations were performed at the Geryon cluster at PUC. JP thanks Conicyt, Fondap and Mecesus for financial support. RJ and PP thank the EU and MICINN for their continuous financial support.

REFERENCES

- Abel T., Bryan G. L. & Norman M. L., 2000, *ApJ*, 540, 39
 Abel T., Bryan G. L. & Norman M. L., 2002, *Science*, 295, 93-98
 Bromm V., Coppi P. & Larson R. B., 1999, *ApJ*, 527, L5
 Bromm V., Coppi P. & Larson R. B., 2002, *ApJ*, 564, 23
 Clark, P. C., Glover, S. C. O., Klessen, R. S., & Bromm, V. 2011, *ApJ*, 727, 110
 Eisenstein D. J. & Hut P., 1998, *ApJ*, 498, 137
 Federrath, C., Duval, J., Klessen, R. S., Schmidt, W., & Mac Low, M. -. 2009, arXiv:0910.5469
 Galli D. & Palla F., 1998, *A&A*, 335, 403
 Glover S. C. O. & Abel T., 2008, *MNRAS*, 388, 1627
 Greif T. H., Johnson, Jarrett L., Klessen R. S. & Bromm, V., 2008, *MNRAS*, 387, 1021
 Kritsuk A. G., Norman M. L. & Padoan P., 2006, *ApJ*, 638L, 25
 Kritsuk, A. G., Norman, M. L., Padoan, P., & Wagner, R. 2007, *ApJ*, 665, 416
 Kritsuk, A. G., Ustyugov, S. D., Norman, M. L., & Padoan, P. 2009, arXiv:0912.0546
 Larson, R. B. 1979, *MNRAS*, 186, 479
 Larson, R. B. 1981, *MNRAS*, 194, 809
 McGreer I. & Bryan G., 2008, *ApJ*, 685, 8
 Nordlund, Å., & Padoan, P. 2003, *Turbulence and Magnetic Fields in Astrophysics*, 614, 271
 Padoan, P., Nordlund, A., & Jones, B. J. T. 1997, *MNRAS*, 288, 145
 Padoan, P., & Nordlund, Å. 2002, *ApJ*, 576, 870
 Padoan P., Nordlund Å., Kritsuk A. G., Norman M. L. & Li P. Sh., 2007, *ApJ*, 661, 962
 Prunet S. Pichon C., Aubert D., Pogosyan D., Teyssier R. & Gottloeber S., 2008, *ApJS*, 178, 179
 Stancil P. C., Lepp S. & Dalgarno A., 1996, *ApJ*, 458, 401
 Teyssier R., 2002, *A&A*, 385, 337
 Truelove J. K., Klein R. I., McKee Ch. F., Holliman J. H., Howell L. H. & Greenough J. A., 1997, *ApJ*, 489, 179
 Wise J. & Abel T., 2007, *ApJ*, 665, 899
 Yoshida, N., Omukai, K., Hernquist, L., & Abel, T., 2006, *ApJ*, 652, 6